# Ion–Ion Equilibration and Particle Distributions in a 3000 km s<sup>-1</sup> Shock in SN 1006

J. C. Raymond <sup>1</sup> , P. F. Winkler<sup>2</sup>, W. P. Blair<sup>3</sup> , and J. M. Laming <sup>4</sup> 
<sup>1</sup> Harvard-Smithsonian Center for Astrophysics, 60 Garden St., Cambridge, MA 02138, USA
<sup>2</sup> Department of Physics, Middlebury College, Middlebury, VT 05753, USA

Department of Physics and Astronomy, Johns Hopkins University, 3400 N. Charles St., Baltimore, MD 21218, USA

Space Science Division, Naval Research Laboratory Code 7684, Washington, DC, 20375, USA

Received 2017 August 22; revised 2017 November 2; accepted 2017 November 7; published 2017 December 6

### **Abstract**

SN 1006 is the most attractive target for investigating the physics of collisionless shock waves faster than 2000 km s<sup>-1</sup>. We obtained UV and optical spectra and an  ${\rm H}\alpha$  image of a 3000 km s<sup>-1</sup> shock driven by a clump of ejecta that has overtaken the blast wave. It is 500 km s<sup>-1</sup> faster than the filament studied earlier. We find kinetic temperatures of H, He, C, and N that are consistent with being mass proportional, suggesting little or no energy transfer among species. We also find evidence that the electron temperature is less than 10% of the proton temperature and that the velocity distribution of H atoms is non-Maxwellian. We measure a proper motion of 0."34  $\pm$  0."01 yr<sup>-1</sup> for the bow shock, which implies a distance to SN 1006 of 1.85  $\pm$  0.25 kpc, and we discuss the role of plasma turbulence in determining the shape of the velocity distribution.

Key words: ISM: individual objects (SN 1006) - ISM: supernova remnants - plasmas - shock waves -

ultraviolet: ISM

#### 1. Introduction

Shock waves mediated by collisions among particles produce thermal equilibrium downstream, with all the particle species having Maxwellian velocity distributions at the same temperature. Collisionless shocks in plasmas, which are mediated by interactions of particles with electromagnetic fields and plasma turbulence, do not necessarily produce thermal equilibrium downstream. Observations of shocks in the solar corona (Raymond et al. 2000; Mancuso et al. 2002), the solar wind (Schwartz et al. 1988; Korreck et al. 2007), and supernova remnants (SNRs; Raymond et al. 1995; Ghavamian et al. 2013) often show that electrons are cooler, and heavier ions hotter, than protons. They also sometimes show power-law tails in the velocity distributions. At the high temperatures and low densities of SN 1006, the Coulomb collision times are of order 80,000 yr, so the shocks are indeed collisionless.

A shock wave converts much of the bulk kinetic energy of the particles it encounters into thermal energy. In the case of a strong shock, the flow speed relative to the shock is reduced by a factor of 4 and the kinetic energy by a factor of 16, so 15/16 of the bulk kinetic energy of each species is converted to thermal energy. Since the kinetic energy is proportional to mass, the different particle species will have mass-proportional temperatures if there is no energy transfer among species. That would lead to extremely low electron temperatures,  $T_e$ , and ion temperatures for He, C, N, and O that are respectively 4, 12, 14, and 16 times higher than the proton temperature,  $T_p$ . Various mechanisms have been proposed that provide some electron heating by plasma waves (Cargill & Papadopoulos 1988; Ghavamian et al. 2007b), driving  $T_e/T_p$  closer to 1, and there are relatively extensive observational data on  $T_e/T_p$  from the solar wind shocks and shocks in SNRs (Ghavamian et al. 2013).

It might be thought that  $T_i/T_p$  could range from 1.0 (complete thermal equilibration) to  $m_i/m_p$  (no equilibration, where all species have the same thermal speeds), but waveparticle interactions produce ion temperatures above mass proportional,  $T_i/T_p > m_i/m_p$  in collisionless plasma in the

upper solar corona (Kohl 1997), and in low collisionality intervals in the solar wind,  $T_i/T_p$  averages 1.35  $m_i/m_p$  (Tracy et al. 2016). Korreck et al. (2007) and Berdichevsky et al. (1997) measured the heating as a function of charge-to-mass ratio in shocks in the solar wind, and they found preferential heating of low Q/M species.

Ion temperatures have been measured in only a few SNR shocks, and they range from nearly equal proton and ion temperatures in a 350 km s<sup>-1</sup> shock in the Cygnus Loop (Raymond et al. 2015a) to nearly mass-proportional temperatures in a 2500 km s<sup>-1</sup> shock in SN 1006 (Raymond et al. 1995; Korreck et al. 2004). Some theoretical studies of ion heating suggest that  $T_i$  should be modestly higher than  $T_p$  (Fuselier & Schmidt 1997), while others predict selective heating and higher than mass-proportional temperatures (Zimbardo 2011).

It is difficult to diagnose the microphysics of distant shock waves such as those in SNRs, but some insights are possible. If a shock passes through partially neutral gas, it produces Balmer line emission whose two- or three-component profile can be used to infer the post-shock proton temperature, the electron-to-proton temperature ratio,  $T_e/T_p$ , and signatures of precursors due to cosmic rays and neutrals returning upstream in the flow (Raymond 1991; Heng 2010; Morlino et al. 2012). This comes about because neutrals are not immediately affected by the shock, so collisional excitation produces a narrow component with the upstream velocity distribution and perhaps an intermediate component affected by a shock precursor. Charge transfer produces a population of neutrals with something like the downstream proton distribution (Chevalier & Raymond 1978; Chevalier et al. 1980).

The blast wave in the SN 1006 SNR is an especially good target for studies of the physics of collisionless shocks. The shocks in SN 1006 are faster than 2000 km s<sup>-1</sup>, the remnant is large in angular size and well resolved, synchrotron X-rays in some parts of SN 1006 show efficient particle acceleration and magnetic field amplification, and the reddening is small enough to permit UV observations (Bamba et al. 2003). It provides one of the highest shock speed  $(V_S)$  examples for studies of

electron—ion temperature equilibration (van Adelsberg et al. 2008) and ion—ion thermal equilibration (Korreck et al. 2004).

In several places, knots of ejecta have overtaken the blast wave in SN 1006, creating distinctive bow shocks moving faster than the local blast wave speed. Katsuda et al. (2013) and Winkler et al. (2014) pointed out a bow shock on the NW rim of SN 1006 whose proper motion indicates a shock speed about 500 km s<sup>-1</sup> faster than the shock studied by Ghavamian et al. (2002) and Korreck et al. (2004). This bow shock is also remarkable because, while no synchrotron X-ray emission is seen along the NW rim where  $H\alpha$  is brightest, a small patch of synchrotron X-ray emission is visible about 30" ahead of the bow shock. We have acquired an optical spectrum from the Magellan Baade telescope at Las Campanas Observatory and a UV spectrum with Cosmic Origins Spectrograph (COS) on HST to measure the electron, ion, and proton temperatures in this  $\sim 3000$  km s<sup>-1</sup> shock.

We find that the velocity widths of the H $\alpha$ , He II  $\lambda$ 1640, and C IV  $\lambda 1550$  lines are consistent with the same value, indicating mass-proportional temperatures. The H $\alpha$  profile is inconsistent with a Gaussian, which implies a non-Maxwellian velocity distribution, and we discuss possible interpretations in Appendix A and the relationship between the spectrum of plasma turbulence and velocity distribution in Appendix B. The observed distribution could be due either to the velocity dependence of the  $\mathrm{H^{+}}$  + H charge transfer cross section or to a nonthermal proton distribution such as a  $\kappa$  distribution. Comparison of the proper motion with the shock speed derived from the  $H\alpha$  profile yields a distance to SN 1006 of  $1.85 \pm 0.25$  kpc, which is consistent with estimates for another part of the  $H\alpha$  filament and with upper and lower limits obtained by other means. We briefly discuss the theory of ionion temperature equilibration and the formation of Maxwellian distributions in collisionless shocks.

#### 2. SN 1006: Background and Previous Work

SN 1006 is one of the most extensively studied SNRs in spite of the fact that it is relatively faint at optical wavelengths. Winkler et al. (2003) estimated a distance of 2.2 kpc based on a  $0.280 \pm 0.008 \text{ yr}^{-1}$  proper motion of the H $\alpha$  filaments in the NW and an assumed shock speed of 2890 km s<sup>-1</sup> from Ghavamian et al. (2002). However, more recent models of the relation between  $H\alpha$  line width and shock speed (Morlino et al. 2013a) indicate that the 2290  $\pm$  80 km s<sup>-1</sup> line width observed by Ghavamian et al. (2002) corresponds to  $V_S = 2500 \pm$ 180 km s<sup>-1</sup>, assuming  $T_e/T_p = 0.05$  and no thermal equilibration among protons and ions, and assuming that the energy going into cosmic rays is negligible at this position. That shock speed implies a distance of  $1.84 \pm 0.14$  kpc. Winkler et al. (2003) pointed out that the ejecta velocity measured by Hamilton et al. (1997), combined with the age and angular size of the SNR, gives a lower limit to the distance of 1.6 kpc, which is compatible with the range obtained from the proper motion and shock speed.

Both the size and low luminosity of SN 1006 are attributed to a low ambient density, since it is 14°.6 off the Galactic plane (470 pc at a distance of 1.8 kpc). The NE and SW sectors are seen in X-ray synchrotron emission and  $\gamma$ -rays (Koyama et al. 1995; Tanimori et al. 1998), while the shock seems to be

encountering denser gas in the NW, where it is seen in thermal X-rays and  $H\alpha$  (Long et al. 2003; Winkler et al. 2014). The interior is filled with exceedingly faint, fluffy X-ray emission from the shocked ejecta, and both the unshocked ejecta and the reverse shock have been detected in absorption lines toward a background star (Wu et al. 1983; Hamilton et al. 2007). The top two panels of Figure 1, both from Winkler et al. (2014), show an  $H\alpha$  image from the CTIO 4 m Blanco telescope and an X-ray image from *Chandra*.

Henceforth, we will assume that the shock speed in the main NW H $\alpha$  filament is  $\sim$ 2500 km s<sup>-1</sup>, based on the H $\alpha$  profile and the model of Morlino et al. (2013a). The ratio of X-ray to optical proper motions indicates shock speeds of around 4000 km s<sup>-1</sup> in the X-ray-synchrotron-dominated rims to the NE and SW (Katsuda et al. 2013; Winkler et al. 2014). Both  $H\alpha$  profiles and X-ray spectra indicate low electron-ion equilibration,  $T_e/T_p \sim 0.05$  in the northwestern filament (Long et al. 2003; van Adelsberg et al. 2008; Nikolić et al. 2013). There is no direct measurement of the ambient magnetic field, but the overall barrel-shaped geometry of the X-ray and  $\gamma$ -ray emission and the pattern of radio polarization favor a field in the NE-SW direction and acceleration in quasi-parallel shocks in those locations on the shell (Rothenflug et al. 2004; Schneiter et al. 2017; Velázquez et al. 2017). This indicates that the shocks in the NW H $\alpha$  filament should be quasiperpendicular.

The low reddening toward SN 1006, E(B-V) < 0.11(Schweizer & Middleditch 1980), makes UV and soft X-ray observations feasible. Far-UV (FUV) observations with the Hopkins Ultraviolet Telescope (HUT) and Far-Ultraviolet Spectroscopic Explorer (FUSE) have indicated roughly massproportional ion/proton temperature ratios,  $T_i = (m_i/m_p)T_p$ (Raymond et al. 1995; Korreck et al. 2004). The XMM grating X-ray spectrum of a bright ejecta knot that has overtaken the main blast wave in the NW also shows a modest electron temperature and a very high oxygen kinetic temperature,  $T_e/T_O \sim 0.005$  (Vink et al. 2003; Broersen et al. 2013). The lack of ion-ion thermal equilibration may be related to the lack of electron-ion equilibration, in the sense that both indicate an absence of plasma turbulence that transfers energy among species. Ion-ion thermal equilibration has been studied in only two other SNRs: the Cygnus Loop, with  $V_{\rm S} \sim 350~{\rm km~s^{-1}}$  and nearly equal proton, helium, carbon, and oxygen temperatures (Raymond et al. 2015a), and DEM L71 in the LMC, with  $V_{\rm S} \sim 900 \ {\rm km \ s^{-1}}$  and  $T_{\rm O}$  intermediate between  $T_p$  and the massproportional value (Ghavamian et al. 2007a).

Katsuda et al. (2013) and Winkler et al. (2014) drew attention to the bow shock visible in  $H\alpha$  that is driven by the ejecta knot that Vink et al. (2003) and Broersen et al. (2013) had studied. Its X-ray proper motion, measured by Katsuda et al. (2013), indicates a higher shock speed than in most of the NW filament, and as we show below, the  $H\alpha$  proper motion indicates a speed over 20% larger than in the region observed by Ghavamian et al. (2002), Raymond et al. (1995), and Korreck et al. (2004). Thus, it provides the opportunity to investigate the electron—ion and ion—ion equilibration in a faster shock.

Both Katsuda et al. (2013) and Broersen et al. (2013) noted the presence of a hard X-ray clump upstream of the bow shock—at least as seen in projection. Broersen et al. (2013) show a spectrum of this clump that shows that its

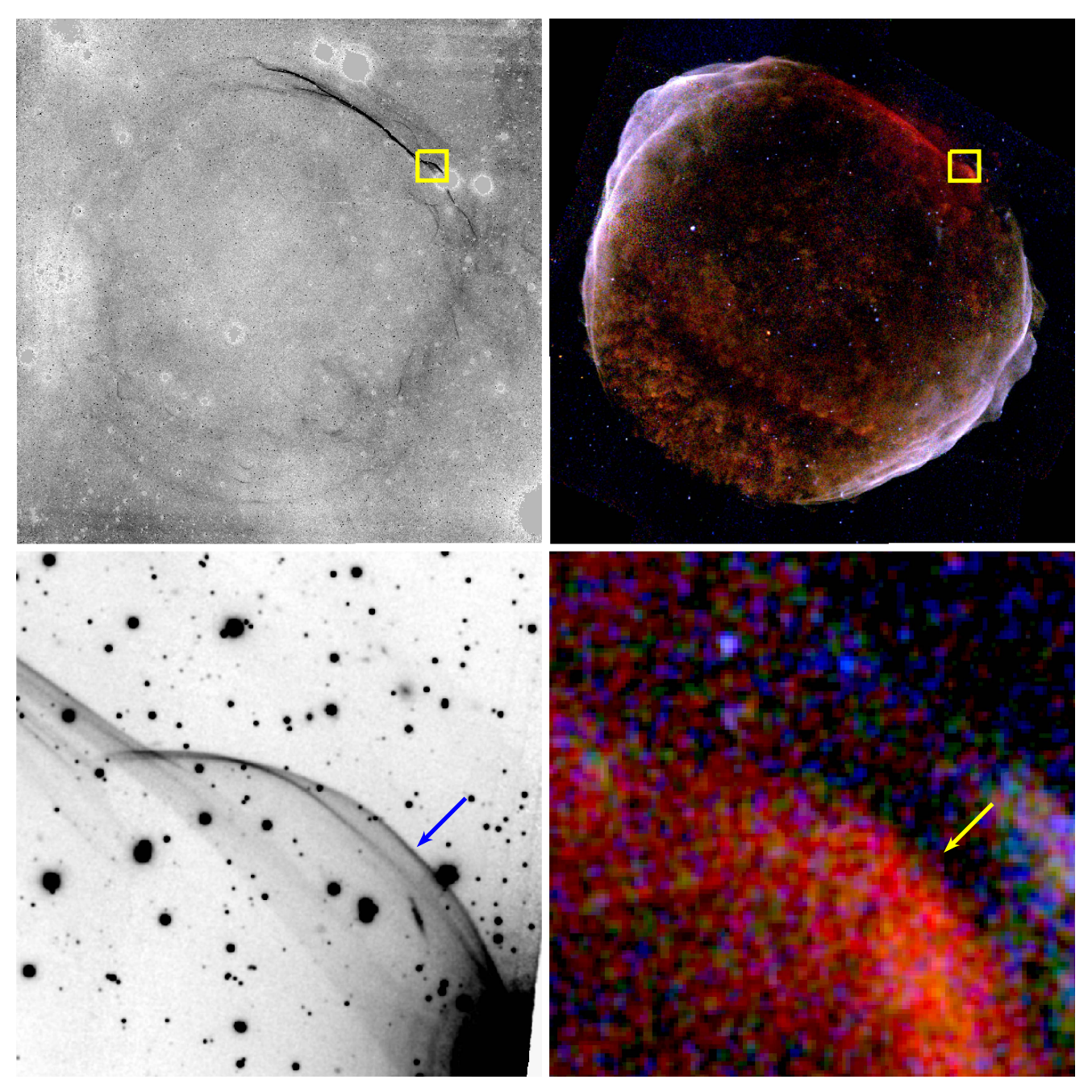


Figure 1. Top left:  $H\alpha$  image of SN 1006, after continuum subtraction, taken from the 4 m Blanco telescope at CTIO in 2010. Top right: 2012 color X-ray mosaic image from *Chandra* (red = 0.5–1.2 keV; green = 1.2–2.0 keV; blue = 2.0–7.0 keV). Both are from Winkler et al. (2014); the small yellow box indicates the region with the bow shock filament, enlarged in the bottom two panels. Bottom left: 120" square section from the  $H\alpha$  image of the bow shock region, taken with GMOS on the 8.2 m Gemini-S telescope in 2015. Bottom right: same section as in the bottom left panel, but from the 2012 *Chandra* image above. The arrow indicates the position along the shock where the COS spectra were taken. All panels are oriented north up, east left. Note that background galaxies are apparent in the bottom left  $H\alpha$  image—an indication of the low absorption on this line of sight that makes UV spectroscopy feasible.

X-ray emission is primarily nonthermal—dramatically different from the thermal emission along most of the NW rim of SN 1006. Katsuda et al. (2013) measured the X-ray proper motion for both the nonthermal clump (their region NT1) and the ejecta knot driving the bow shock (their region T1) as  $0\rlap.{''}48\pm0\rlap.{''}05\pm0\rlap.{''}03~yr^{-1}$  and  $0\rlap.{''}32\pm0\rlap.{''}03\pm0\rlap.{''}03~yr^{-1}$ , respectively (uncertainties are statistical and registration). It is not clear whether there is any physical relationship between the nonthermal X-ray knot and the bow shock. All of these features are illustrated in the various panels of Figure 1.

# 3. Observations

We obtained new imaging data of the NW limb of SN 1006, as well as optical long-slit and HST COS FUV spectroscopy taken at a position near the apex of the ejecta knot bow shock, chosen in order to avoid the complication of oblique shocks that occur in bow shock wings. The position we chose for spectroscopy is indicated in the bottom panels of Figure 1 and

<sup>&</sup>lt;sup>5</sup> In oblique shocks the effective shock speed is lower than at the apex, and there may be bulk motions—required to conserve the parallel component of incident velocity—that can affect the line width.

Table 1					
$H\alpha$ Imaging	Observations	of SN	1006		

Date (UT)	Telescope	Instrument	Scale (" pixel <sup>-1</sup> )	Exposure (s)	Seeing (FWHM)
1998 Jun 23	CTIO 0.9m	Tek2K#3	0.401	6 × 1000	1."3
2002 Mar 21	CTIO 0.9 m	Tek2K#3	0.401	$4 \times 1000$	1."1
2006 Mar 30-Apr 3	CTIO 0.9 m	Tek2K#3	0.401	$6 \times 1000$	1."7
2010 Apr 15–18	CTIO 4 m	Mosaic2	0.269	$12 \times 600$	1."1
2015 Apr 14	Gemini-S 8.1 m	GMOS	0.146	$5 \times 250$	0."6
2016 Apr 30–May 1	Magellan I 6.5 m	IMACS	0.111	5 × 600	0."6

is located about 4.'3 W and 2.'9 S of the position on the smooth part of the SN 1006 H $\alpha$  filament observed by Ghavamian et al. (2002) and Korreck et al. (2004). It is also SW of the regions covered by the ACS H $\alpha$  image of Raymond et al. (2007) and the VIMOS Integral Field Unit (IFU) H $\alpha$  observations of Nikolić et al. (2013). Below, we describe each of these new observations in more detail.

# 3.1. Imaging Observations

In order to accurately specify a position for the COS spectra, we obtained an image of the bow shock region with the GMOS instrument on the 8.2 m Gemini South telescope in 2015 April. Because the proper motion is significant along the entire NW filament of SN 1006, we used an image we had obtained in 2010 April from the 4 m Blanco telescope at CTIO to compare with the later image and obtain a proper-motion measurement sufficiently accurate to specify a position for the 2".5 COS aperture. As a further check, we obtained an  $H\alpha$  image from the IMACS instrument on the 6.5 m Magellan I (Baade) telescope on 2016 April 30 and May 1, during the same run that was mostly devoted to spectroscopy of the filament (Section 3.2). Subsequently, we have used data from these three observations, together with archival images from three earlier observing runs in 1998, 2002, and 2006, to obtain a more definitive proper-motion measurement (Section 4.1). Table 1 gives a journal of all the observations used for this measurement. The images from 2002, 2010, and 2015 are superposed in Figure 2 to show the proper motion.

#### 3.2. Magellan/IMACS Spectra

Deep optical spectra, at nearly the same position as the COS UV spectra, are necessary in order to obtain Balmer line profiles —especially the width of the H $\alpha$  broad line component. We obtained such spectra, also with the IMACS instrument and f/4 camera at Magellan I (Baade), on the nights of 2016 April 30 and May 3 (UT). We placed a slit of width 1".5 along the apex of the bow shock filament. We used the blue-blazed 600 line mm<sup>-1</sup> grating, with a range of tilts to easily cover the H $\beta$  and H $\gamma$  lines in addition to H $\alpha$ . For the night of April 30 the detector was binned  $\times 4$  in the dispersion direction to give a dispersion of 1.51 Å pixel<sup>-1</sup>, while on the night of May 3 the binning was  $\times 2$  (0.76 Å pixel<sup>-1</sup>). The detector was binned  $\times 2$  in the spatial direction on both nights, for a scale of 0."22 pixel<sup>-1</sup>. Figure 3 shows the IMACS slit position, as well as the positions for the COS aperture (Section 3.3).

On the night of April 30, we took three  $1000 \text{ s } 4 \times 2$ -binned exposures at each of five grating tilts, for a total exposure time

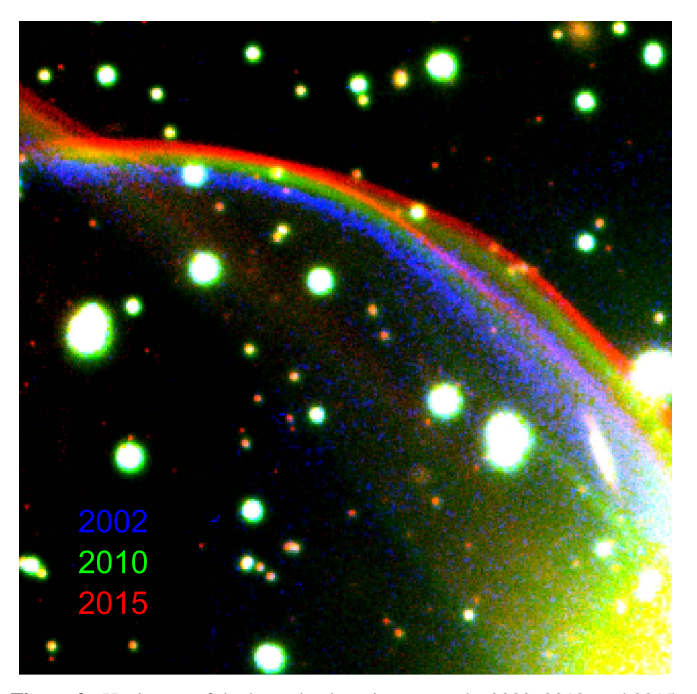


**Figure 2.** H $\alpha$  image of the bow shock region at epochs 2002, 2010, and 2015, shown in blue, green, and red, respectively. The field is 80" square and is oriented N up, E to the left. The bow shock filament's large proper motion to the NW is apparent.

of 15,000 s, under photometric conditions. On May 3 we used  $2 \times 2$  binning and took three 1200 s exposures at each of five tilts, plus another  $3 \times 1000$  s at a sixth tilt, for a total exposure time of 21,000 s. Throughout this night we experienced variable cirrus clouds.

The initial processing was done in the COSMOS environment and included overscan correction, trimming, bias subtraction, and stitching together the separate files from the eight detector chips for each frame. We then used the COSMOS task extract-2dspec to strip out the 2D spectrum. From this point, we used IRAF for the subsequent processing, including flat-fielding, combining multiple frames at each tilt, wavelength calibration, and finally combining the data with different tilts to produce a combined 2D spectrum. (For grating tilts where a chip gap interrupted the spectrum near either  $H\alpha$  or  $H\beta$ , we excluded data with that tilt.) We then used blank-sky regions at either end of the slit to fit and subtract the sky in the 2D spectrum, and we summed the lines showing emission from

<sup>&</sup>lt;sup>6</sup> The GMOS image was obtained under the previously allocated program GS-2015A-Q-72.

Software from the Carnegie Observatories, available at http://code.obs.carnegiescience.edu/cosmos.

<sup>8</sup> IRAF is distributed by the National Optical Astronomy Observatory, which is operated by the Association of Universities for Research in Astronomy, Inc., under cooperative agreement with the National Science Foundation.

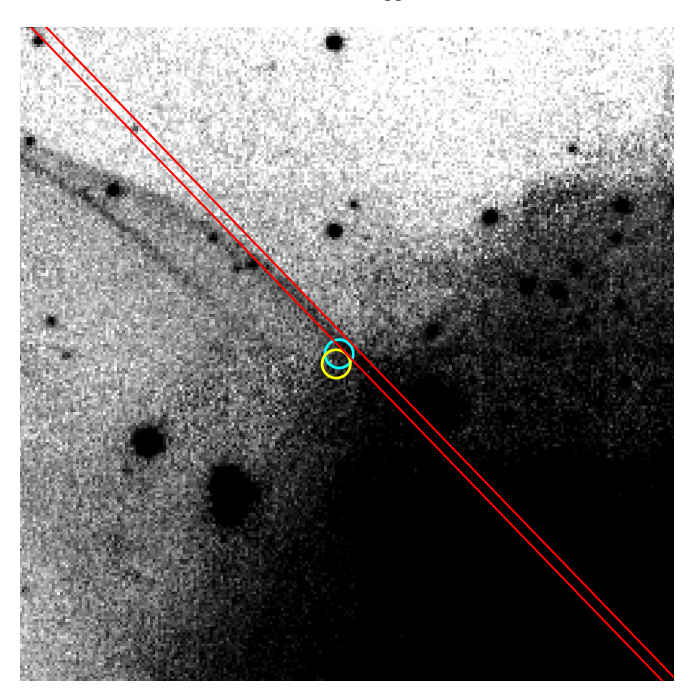


Figure 3. H $\alpha$  image of the bow shock region taken with Magellan/IMACS during the same 2016 observing run when the optical spectra were obtained. The tilted red lines indicate the position of the 1".5 IMACS slit; the cyan circle denotes the COS aperture position at visit 1, while the yellow circle is the position at visits 2 and 3. The image is 60" square and is oriented N up, E to the left. This image has a great deal of scattered light from the bright star HD 132689, with V=8.3, located just out of the field to the SW.

the bow shock filament to extract a 1D spectrum. We achieved flux calibration based on our long-slit observations of several spectrophotometric standard stars from the list of Hamuy et al. (1992).

The flux-calibrated 1D spectrum for the bow shock filament is shown in Figure 4. Note that  $H\alpha$  and  $H\beta$  clearly display both broad and narrow components. All the other features visible are imperfectly subtracted night-sky lines. The faint continuum is a combination of hydrogen two-photon emission and scattered starlight. The  $H\alpha$  and  $H\beta$  profiles are shown in Figures 5 and 6 along with the fits discussed below.

## 3.3. HST/COS

A total of 15 *HST* orbits were devoted to COS FUV observations as part of a Cycle 24 GO program 14228. The data were obtained on 2016 July 2, July 10, and August 14. For the first observation we observed the position indicated in cyan in Figure 2 with the COS 2"5-diameter Primary Science Aperture and the G140L grating. The position was chosen to be about 0"6 behind the H $\alpha$  filament determined from images from 2010 (Winkler et al. 2014) based on theoretical estimates of the spatial distributions of He II, C IV, and N V emission behind the shock and the assumed proper motion of the filament. Those estimates were based on the ionization timescales and the flow speed behind the shock, so they depended on assumed values for the shock speed, pre-shock density, and electron temperature and are therefore uncertain by up to a factor of 2, or about 1/2 the aperture diameter.

Based on the Magellan image described above, we adjusted the pointing for the latter two observations slightly (about 1''), partly to test for small-scale spatial variations. The geocoronal Ly $\alpha$  varied by a factor of 2 among the three dates, and the

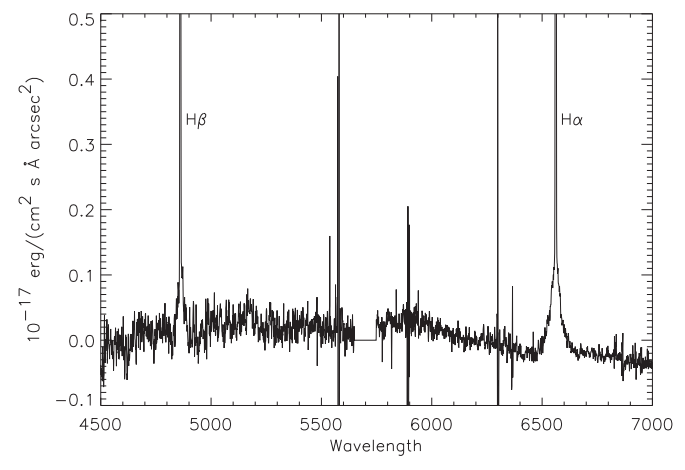


**Figure 4.** Full Magellan/IMACS spectrum of the bow shock. The broad components on  ${\rm H}\alpha$  and  ${\rm H}\beta$  are visible, and the narrow components go off-scale in this figure. Very faint scattered background starlight is visible across the entire spectrum.

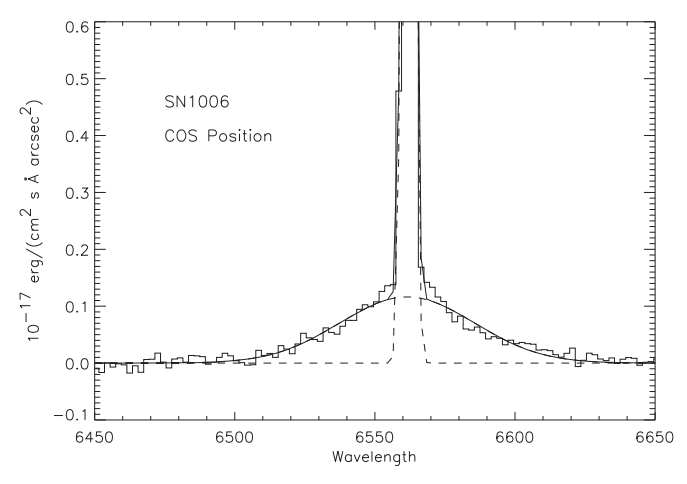
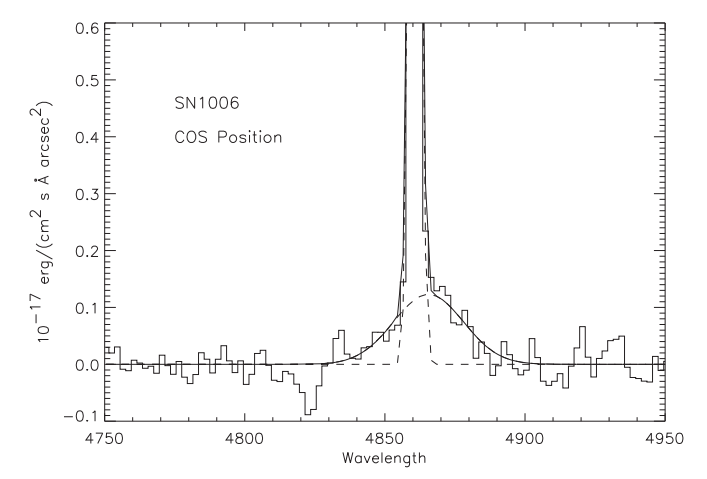


Figure 5. Enlargement of the  $H\alpha$  profile of the bow shock in SN 1006. The broad and narrow Gaussian components are shown as dashed lines, and their sum is shown as a solid line. The histogram shows the data.



**Figure 6.** H $\beta$  profile of the bow shock in SN 1006. The broad and narrow Gaussian components are shown as dashed lines, and their sum is shown as a solid line. The histogram shows the data.

geocoronal O I  $\lambda$ 1304 line varied by about 15%, but there was no detectable difference among the fluxes or widths of the SNR emission lines detected at C IV  $\lambda$ 1550 and He II  $\lambda$ 1640.

**Table 2** *HST*/COS Observations

Date	R.A. (J2000.)	Decl. (J2000.)	Orientation <sup>a</sup>	Exposure (s)
2016 Jul 2	15 <sup>h</sup> 01 <sup>m</sup> 51. 1388	-41° 48′ 16″49	-28°.80	14991
2016 Jul 10	15 <sup>h</sup> 01 <sup>m</sup> 51. 1630	-41° 48′ 17″42	-54°.00	14991
2016 Aug 14	15 <sup>h</sup> 01 <sup>m</sup> 51 <sup>s</sup> 1630	-41° 48′ 17″42	-48°.88	14990

#### Note.

Therefore, we combined the data from all three visits for a total of 45 ks. The observational details are listed in Table 2.

The orientations of the COS instrument relative to the filament also differed among the three observations. If the emission uniformly fills the aperture, this has no effect on the observed line profiles, but if the aperture is only partially filled in the dispersion direction, the profiles will be narrower than if the aperture is filled. On August 14, the dispersion direction was close to eastwest, and for the other visits it was 16° and 9° from east to west, so that in all cases the filament was roughly 45° from the dispersion direction, and partial filling of the aperture thus should not have a significant effect on the line profile. Also, the observed line widths are twice the instrumental width, so any effect cannot be very large.

The derived, calibrated spectrum is shown in Figure 7. Expanded plots of the He II, C IV, and N V lines are shown in Figure 8 and 9. The brightest features are the geocoronal Ly $\alpha$  and O I  $\lambda$ 1304 lines. The feature near 1360 Å contains geocoronal O I]  $\lambda$ 1356, but a possible line near 1380 Å is not in lists of expected geocoronal features (Meier 1991). There is a faint N<sub>2</sub> line at 1386 Å, but other N<sub>2</sub> lines are not seen. It could possibly be O V  $\lambda$ 1371 from the shock, but it is 10 times brighter relative to C IV than expected based on the collision strengths and ionization rates from the CHIANTI database (Del Zanna et al. 2015).

There is a discernible continuum throughout the COS spectral range. This cannot be the two-photon continuum from decay of the metastable 2s level of H I, since that would peak at around  $1450\,\text{Å}$  and drop toward zero as the wavelength approaches  $\text{Ly}\alpha$ , which is not observed. Rather, it is dust-scattered galactic background starlight, as also seen with HUT (Raymond et al. 1995). That continuum was attributed to dust-scattered light from B stars based on a private communication from J. Murthy, whose UV background observations showed that this area of the sky is unusually bright.

# 4. Analysis

#### 4.1. Proper Motion

We have used  ${\rm H}\alpha$  images for six epochs from 1998 to 2016, as listed in Table 1, to measure the proper motion of the Balmer filament that delineates the bow shock. All the images were first placed on a common world coordinate system using a few hundred stars from the *Gaia* First Data Release (Gaia Collaboration et al. 2016). We then extracted a 1D profile for each epoch from a section 8" long, oriented normal to the shock front at the bow shock position. For each epoch pair separated by  ${\sim}4$  yr or more, we carried out a  ${\chi}^2$  fitting procedure to determine the proper motion over the intervening interval—a total of 14 independent epoch pairs. Since the 2015 and 2016 images had significantly better seeing than those at the earlier epochs, it was necessary to smooth the sharper images with an

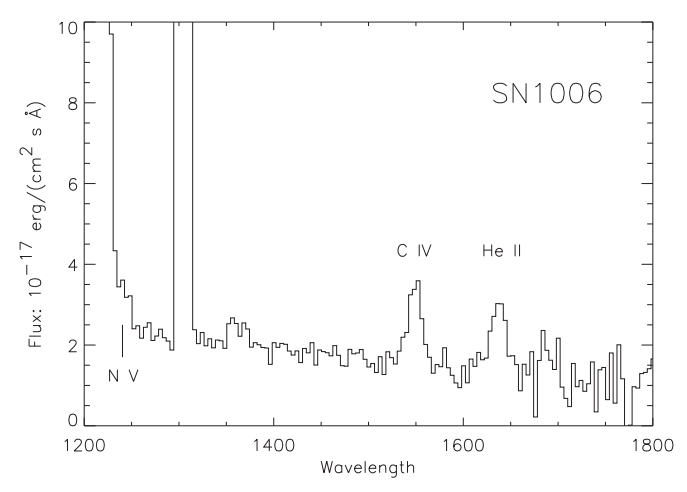


**Figure 7.** Calibrated UV spectrum from COS/G140L. Lines of C IV and He II are from the SNR shock. Geocoronal Ly $\alpha$   $\lambda$ 1215, O I  $\lambda$ 1304, and OI]  $\lambda$ 1356 are visible, as well as a possible unidentified feature at 1380 Å.

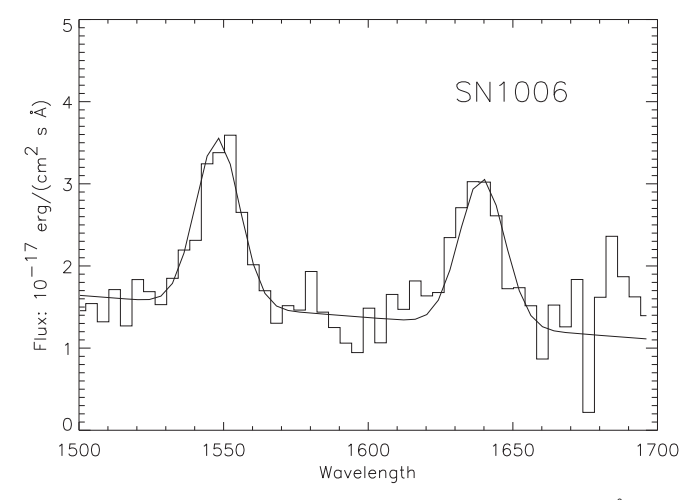
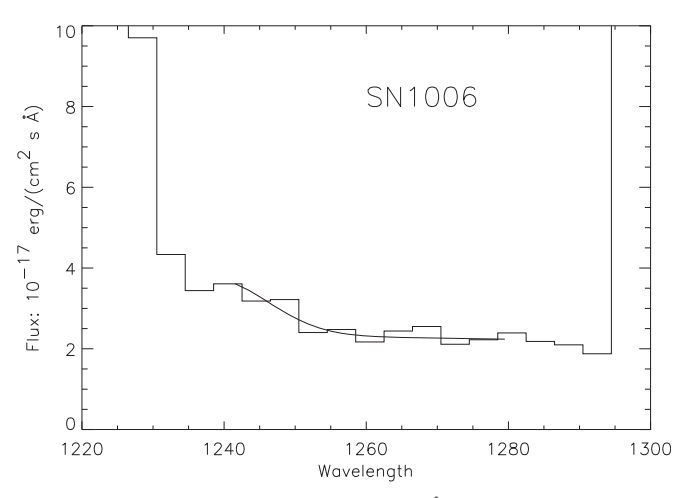


Figure 8. Enlargement of the COS spectrum between 1500 and 1700  $\mathring{\rm A}$  with a best-fit curve shown.

appropriate Gaussian to obtain acceptable fits. Figure 2 shows the bow shock region at three of the epochs, displayed in different colors.

All the epoch pairs gave reasonably good fits and results ranging from  $0.314 \pm 0.019 \, \mathrm{yr^{-1}}$  to  $0.357 \pm 0.023 \, \mathrm{yr^{-1}}$ , with most of the pairs ranging from  $0.336 \, \mathrm{yr^{-1}}$  to  $0.349 \, \mathrm{yr^{-1}}$ . We took a simple average of all 14 measurements to obtain our final result for the proper motion of bow shock filament:  $0.341 \pm 0.010 \, \mathrm{yr^{-1}}$ , where the uncertainty should include both statistical errors and possible systematic ones due to misalignment of images from different epochs. This corresponds to  $-0.245 \pm 0.08 \, \mathrm{yr^{-1}}$  in R.A. and  $+0.238 \pm 0.08 \, \mathrm{yr^{-1}}$  in decl.

<sup>&</sup>lt;sup>a</sup> Spacecraft orientation, which determines the dispersion direction of COS.



**Figure 9.** COS spectrum between 1220 and 1300 Å shown with a fit to the faint continuum plus an assumed N V  $\lambda$ 1240 line. The strong geocoronal Ly $\alpha$  and O I dominate at left and right.

This value is 22% faster than the proper motion of 0."280 yr $^{-1}$  obtained by Winkler et al. (2003) for the brighter main portion of the NW filament in SN 1006, located a few arcminutes to the NE. It is hardly surprising that the bow shock region is moving faster, since the shock is apparently being driven ahead here by an ejecta fragment. Indeed, it was for this reason that we selected it for study with COS—to study the fastest shock that was also bright enough to enable us to obtain an ultraviolet spectrum in a reasonable amount of time. Combining our proper motion with the distance of 1.84  $\pm$  0.14 kpc from the proper motion and shock speed of the main NW filament, we obtain a shock speed of 3030  $\pm$  250 km s $^{-1}$  for the bow shock.

Our long sequence of images will enable a more complete study of the proper motions of optical filaments in SN 1006, which will be reported in a separate publication.

# 4.2. Optical Spectrum

We extracted the spectrum of a 15" section of the IMACS slit centered on the HST/COS position, using regions outside the extracted area for background, and avoiding stars and scattered starlight to the southwest of the extracted region. Although this extraction region is larger than the 2".5 COS aperture, we do not expect (nor can we see) significant changes over this region, and we found the larger extraction region necessary to obtain sufficient signal-to-noise ratio on this exceedingly faint emission. The H $\alpha$  and H $\beta$  profiles were fit with two Gaussians plus sky background. The backgroundsubtracted H $\alpha$  and H $\beta$  profiles are shown separately in Figure 5 and 6. We tried binning the data to improve the signal-to-noise ratio further in the line wings, and the H $\alpha$  fit uncertainties listed in Table 3 were obtained with the data binned by 4 Å. We also extracted different portions of the 15" region that shows H $\alpha$  to search for variations along the slit. Those subregions yielded the same parameters, but with larger uncertainties. The results of the fits are shown in Table 3.

The fits give an  $H\alpha$  width of 2590 km s<sup>-1</sup>, with an uncertainty of about  $\pm 180$  km s<sup>-1</sup>, and an intensity ratio of the broad to narrow components of 0.49  $\pm$  08. From Equation (3) of Morlino et al. (2013a) the width implies a shock speed of  $3060 \pm 400$  km s<sup>-1</sup>, in excellent agreement with the value of  $3030 \pm 250$  km s<sup>-1</sup> obtained from the proper motion and the distance obtained from the shock speed and proper motion of

the filament observed by Ghavamian et al. (2002). The shock velocity from the H $\alpha$  profile and the proper motion of the bow shock imply a distance of  $1.85 \pm 0.25\,\mathrm{kpc}$ . It should be recalled that the models assume that  $T_e/T_p = 0.05$ , that there is no thermal equilibration among protons and ions, and that the energy going into cosmic rays is not significant. Since the broad component line width basically measures the proton temperature and any energy given to the electrons or cosmic rays is taken from the protons, the shock speed estimate would be increased by about a factor of  $(1 + T_e/T_p)^{1/2}$  or  $(1 + 8\epsilon/9)^{1/2}$ , where  $\epsilon$  is the fraction of the energy dissipated in the shock that goes into cosmic rays. On the other hand, since the He ions carry four times as much kinetic energy as the protons, thermal equilibration among ions would heat the protons and decrease the shock speed estimate by up to 20%. We discuss these possible corrections in Section 5.

It is also important to note that a two-Gaussian fit to the broad and narrow components of  $H\alpha$  is not formally acceptable, with reduced  $\chi^2\sim 9$ . Improper sky subtraction could possibly distort the profile. A contribution from scattered starlight is visible to the west of the bow shock, and it clearly varies both with position along the slit and with wavelength. We tried a range of combinations of sky background from above and below the extraction region and chose the one that produces a zero level for the background-subtracted spectrum for 100 Å beyond the wings on both sides of the H $\alpha$  line. We also used the night-sky lines to verify that the instrument response does not include wings that would artificially broaden the narrow component. We therefore consider it very probable, though not entirely certain, that the broad component is non-Gaussian. We discuss possible interpretations in Section 5 and Appendix A, and we discuss the relationship between plasma turbulence and the formation of a Maxwellian or  $\kappa$  distribution in Appendix B.

We also fit the  $H\beta$  line, though the results are very sensitive to the choice of the background regions and we could not find a really satisfactory background. The broad component width is consistent with that of  $H\alpha$ , but with much larger uncertainties. The Balmer decrement of the narrow component is potentially a useful diagnostic for the efficiency of conversion of  $Ly\beta$  to  $H\alpha$  (Ghavamian et al. 2001), which in turn affects things like the interpretation of the broad-to-narrow intensity ratio in terms of electron temperature. We discuss the Balmer decrement below.

# 4.3. The UV Spectrum

To measure the kinetic temperatures of He, C, and N, we assume Gaussian line profiles and a 2:1 intensity ratio for the doublet lines of C IV and N V. For the Cygnus Loop, the optical depths in the C IV lines are below 1 (Raymond et al. 2015a), and in SN 1006 they should be much smaller still because of the larger line width, because the emission is spread over a wider region on the sky, and because the depth along the line of sight is smaller. We estimate that the optical depth in the strongest line, C IV  $\lambda 1548$ , is less than 0.02. We apply a similar logic to the N V lines. Thus, the C IV and N V lines are optically thin to a very good approximation, and the 2:1 doublet ratio is appropriate.

To assess the statistical noise level in the data, we use the fact that spectra are highly oversampled. We take the noise for each pixel to be the rms of 50 pixels centered on the wavelength of that pixel, or about 1/2 the resolution element.

 Table 3

 Emission-line Fit Parameters: UV Lines and Broad and Narrow Balmer Lines

Ion	$\lambda_0$ (Å)	FWHM (km s <sup>-1</sup> )	Centroid (km s <sup>-1</sup> )	Intensity $(10^{-17} \text{ erg cm}^{-2} \text{ s}^{-1} \text{ arcsec}^{-2})$	$\chi^2_{ u}$	$\frac{T/m}{(10^8 \text{ K/}m_{\text{Ion}})}$
$H\alpha_B$	6563	$2590^{+160}_{-230}$	-59	$7.74 \pm 0.2^{a}$	9.17	2.0 <sup>b</sup>
$H\alpha_N$	6563	0	-41	$14.9 \pm 1.4$		
$H\beta_B$	4861	$2330^{+490}_{-490}$	+260	$2.40 \pm 0.5$	12.1	
$H\beta_N$	4861	0	-10	$6.99 \pm 0.7$		
Не п	1640	$3400^{+2400}_{-1300}$	-620	$7.2 \pm 2.5$	4.64	3.3
C IV	1550	$3000^{+900}_{-800}$	-20	$7.6 \pm 1.4$	2.61	2.6
N V	1240	$4000^{+2500}_{-1200}$	-130	$5.4\pm1.8$	3.98	4.6

#### Notes.

We tested other choices for the width of the interval over which the rms was computed and found that it makes no difference to the best fit and very little difference to the error ranges.

We defined the continuum with a linear fit to the entire 1250–1800 Å wavelength range, excluding geocoronal and SNR emission lines, and used this for the narrower intervals where we fit the lines. As mentioned above, the continuum shape does not match the H I two-photon continuum. Rather, it appears to be scattered light from B stars in that area of the sky.

For each line we convolved a Gaussian with the line profile derived from the observation of a planetary nebula, NGC 6853, whose emission lines are unresolved (Raymond et al. 2015b). Those observations (made with the G160M grating) showed somewhat flat-topped profiles, which we fit with pairs of Gaussians about 100 km s<sup>-1</sup> wide separated by about 100 km s<sup>-1</sup>. For the present analysis we scaled NGC 6853 profile fits by a factor of 6.57, the ratio of dispersions (Å pixel<sup>-1</sup>) of G140L compared to G160M. This gives an instrumental line width of about 6.6 Å, or about 1300 km s<sup>-1</sup> at 1550 Å.

We fit the C IV and He II features and continuum over 100 Å intervals. The N V line is badly blended with geocoronal  $Ly\alpha$  on its short-wavelength side. We fit only the part of the line longward of 1240 Å and fixed the line centroid to the velocity found for a simultaneous fit to the C IV and He II lines. These results are summarized in Table 3.

The reduced  $\chi^2$  values are somewhat larger than expected for Gaussian profiles and purely statistical noise. Part of this seems to be due to some anomalously large deviations in the continuum (e.g., near 1675–1690 Å), which is caused by the decreasing sensitivity at longer wavelengths. It is plausible that the poor quality of the fits is due to departure of the scattered B star continuum shape from the straight line that we assumed, but it could also be due to intrinsically non-Gaussian line profiles. We discuss that possibility further in Appendix A.

The intensities in Table 3 have not been corrected for extinction. The dereddened intensities of the UV lines would be about 2.2 times the observed values for E(B-V)=0.11 (Raymond et al. 1995). The observed fluxes do not reflect the total relative emission per atom in the He II, C IV, and N V lines. We expect that the COS aperture captures essentially all the He II emission from that section of the shock, but the C IV and especially the N V emissions are expected to be more extended than the COS aperture, so that their observed ratios to He II are lower limits. The C IV/He II ratio is predicted to be about 4 assuming that carbon is depleted by a factor of 2 (Laming et al.

1996), while we observe a C IV/He II ratio of 1. Thus, only about 1/4 of the C IV emission falls in the COS aperture, or else carbon is more strongly depleted than assumed by Laming et al. (1996).

We can use the He II flux to estimate the pre-shock density. We estimate the radius of curvature of the bow shock to be  $\sim$ 50" from Figure 2, so a 2" aperture takes in bow shock emission over a length of  $\sim$ 0.3 pc at a distance of 1840 pc. The shock produces 0.0067 He II  $\lambda 1640$  photons per H atom passing though the shock (Laming et al. 1996), and with reddening, one expects  $2.0 \times 10^{-15} n_0 \text{ erg cm}^{-2} \text{ s}^{-1}$ , which would imply that  $n_0$  is about  $0.04 \,\mathrm{cm}^{-3}$ , or about 1/3 the density estimated from the thickness of the filaments observed by HST (Heng et al. 2007; Raymond et al. 2007). On the other hand, a similar calculation for the H $\alpha$  intensity using a 1".5 slit width and 0.2 photons per neutral H atom gives  $n_0 f_0 = 0.025$ , which fits well with the pre-shock density of 0.15-0.3 cm<sup>-3</sup> from Heng et al. (2007) and Winkler et al. (2013) and preshock neutral fraction of 0.1 (Ghavamian et al. 2002). The He II and H $\alpha$  intensities could be reconciled by a higher reddening, or by a smaller radius of curvature in the LOS direction and a higher hydrogen neutral fraction. We think it more likely, however, that the COS aperture intercepted a smaller fraction of the He II emission than we have estimated.

# 5. Discussion

In this section we consider possible corrections to the kinetic temperatures derived above due to Coulomb collisions, bulk motions that could contribute to the line widths, and possible non-Maxwellian velocity distributions. We then compare the kinetic temperature ratios with those observed in other SNR shocks and finally compare theoretical predictions with our results.

#### 5.1. Coulomb Collisions

In their study of the Cygnus Loop, Raymond et al. (2015a) found that Coulomb collisions would push the temperatures toward equilibrium as the gas was being ionized. The Coulomb collision rate scales as  $Z^2/M$ , and the ionization timescale is larger for higher-ionization species such as N V and O VI. The result for the Cygnus Loop was that Coulomb equilibration is insignificant for He, reduces the kinetic temperature of carbon by about 12%, and reduces  $T_0$  even more. For SN 1006, the electron temperature is higher, but the ionization times are not

<sup>&</sup>lt;sup>a</sup> Balmer line brightness for a 15" section of the 1".5 IMACS slit.

b Proton temperature inferred indirectly from the shock speed derived from FWHM and Morlino et al. (2013a, Figure 3).

much different. However, the Coulomb collision time scales as  $T^{3/2}$ , and the ion temperatures are well over an order of magnitude larger. Therefore, Coulomb collisions change the temperatures by at most a few percent in the region where the UV lines are produced, and we do not apply any correction. For example, the proton thermalization time is 80,000 yr, while the time to ionize up to and above N V is about 500 yr.

## 5.2. Bulk Velocity

The second possible correction is the contribution of the lineof-sight (LOS) component of the expansion velocity to the line widths. This would amount to some velocity that should be subtracted in quadrature from each of the line widths. If the observed line widths are the same, the corrected widths would also be the same, but the uncertainty range would be expanded. Shimoda et al. (2015) constructed hydrodynamic simulations of blast waves in a medium with density fluctuations similar to those estimated from turbulence studies of the interstellar medium, and they found that even in smooth-looking filaments the ripples and their associated LOS velocity components caused an increase in line width that could result in a 25% overestimate of the temperatures. In the case of the region we study here, the small size of the COS aperture and the small size of the bow shock probably make this a few percent effect at most because the amplitude of density fluctuations on these small scales should be small.

The bow shock will result in some component of the bulk velocity along the line of sight. Except at the apex of the bow shock, the shock itself is oblique, with a parallel component  $V_{BS}$  sin $\theta$  that is conserved and a perpendicular component  $V_{BS}$  cos $\theta$  that serves as the effective shock speed that determines the post-shock temperature. The LOS component of the parallel velocity is  $V_{BS}$  sin $\theta$  cos $\theta$ . If the bow shock that we observe is cylindrically symmetric, as seems likely for a shock driven by an ejecta knot, the velocity broadening will be roughly  $V_{BS}$  times the 1".25 radius of the COS aperture divided by the  $\sim 50$ " bow shock radius, which again is only a few percent effect.

It is worth noting that the bow shock is not moving exactly in the plane of the sky, so the tangency that defines the optical filament is not exactly at the apex of the bow shock. However, the ratio of the  $-59~\rm km~s^{-1}$  centroid ( $-85~\rm km~s^{-1}$  in the local standard of rest) of the H\$\alpha\$ broad component to the shock speed indicates that the bow shock axis lies only 1 or 2 degrees out of the plane of the sky. This effect can be ignored in our case.

# 5.3. Non-Maxwellian Velocity Distributions

The Gaussian fits shown in Table 3 are not formally acceptable, with reduced  $\chi^2$  values as large as 9 for  $H\alpha$ . For the UV lines, we based the statistical uncertainties in the COS data on the rms variations within a resolution element, but it is possible that the COS response or the UV background contains variations at about the scale of the line width. Therefore, we consider it less certain that the departures from Maxwellian profiles for the UV lines are real.

The  ${\rm H}\alpha$  broad component is probably non-Maxwellian (Section 4.2 and Appendix A). The  ${\rm H}\alpha$  profile is not the same as the proton velocity distribution, but rather it is given by the proton distribution weighted by the product of charge transfer cross section multiplied by velocity. Morlino et al. (2013a) found that for shocks faster than 2500 km s<sup>-1</sup> the rapid decline in the charge transfer cross section with velocity produces

non-Gaussian profiles, though the profiles for a shock viewed edge-on are closer to Gaussian than those viewed face-on (Heng & McCray 2007).

Morlino et al. (2013a) do not indicate how strongly the  $H\alpha$  profile should depart from a Gaussian. The  $H\alpha$  profile in Figure 5 shows extra emission above the Gaussian fit at low velocities on both sides of the peak, along with some extra emission at high velocities on the red wing near 6600 Å. A non-Maxwellian broad component profile was previously reported for a shock in Tycho's SNR (Raymond et al. 2010), and the IFU spectra of SN 1006 (Nikolić et al. 2013) showed a hint of departures from Gaussian profiles. Raymond et al. (2010) listed four potential interpretations of departures from Gaussian profiles: (1) a superposition of different shocks within the instrument field of view, (2) a contribution from neutrals formed by charge transfer with pickup ions (Raymond et al. 2008), (3) a power-law tail on the velocity distribution, or (4) a contribution of emission from a shock precursor.

The shock in Tycho is below 2000 km s<sup>-1</sup>, so the weighting by charge transfer cross section does not explain that profile, but it might well explain the profile of the faster shock in SN 1006. We discuss each of the other possibilities in Appendix A, and we find that either a power-law tail ( $\kappa$  distribution) or emission from a shock precursor is possible, but that the apparently low particle acceleration efficiency in this region makes either seem less likely. Appendix B discusses the relationship between the spectrum of plasma turbulence and the nature of the velocity distribution.

# 5.4. Electron-Ion Equilibration

The intensity ratio of the broad and narrow components is a useful diagnostic for the electron-to-proton temperature ratio (Raymond 1991; Smith et al. 1991; Ghavamian et al. 2000; Morlino et al. 2012, 2013b), though there are significant complications.

One difficulty arises because much of the excitation to the n=3 level produces Ly $\beta$  photons, and those photons can be absorbed by other H atoms and converted to  $H\alpha$ , and the conversion efficiency depends on the optical depth in the Ly $\beta$ line (Chevalier et al. 1980). The ratio  $I_B/I_N$  differs by 40% between Case A (no conversion) and Case B (complete conversion). The Balmer decrement of the narrow component,  $I_N(\alpha)/I_N(\beta)$ , is a diagnostic for the conversion efficiency, though it also depends on the cosmic-ray acceleration efficiency (Shimoda et al. 2017). We measure a narrowcomponent decrement of 2.1  $\pm$  0.3, which becomes 1.9  $\pm$  0.3 after dereddening. For the somewhat slower shock at the position observed by Ghavamian et al. (2002), Shimoda et al. (2017) predict a ratio between 2.9 (Case A) and 3.7 (Case B) if cosmic-ray acceleration is inefficient, or a ratio of 2.3-3.5 if 60% of the shock energy goes into cosmic rays. While the high cosmic-ray prediction is almost compatible with our observation for Case A, reality is likely to be roughly halfway between Cases A and B (Chevalier et al. 1980), and the acceleration efficiency is very high (Section 5.6). There might be a significant calibration uncertainty because the slit was not at the parallactic angle, or the background subtraction might be a problem for the very faint  $H\beta$  line.

There is another complication for the broad-to-narrow ratio if a shock precursor makes a significant contribution to the narrow component intensity. Measurements of proton and electron temperatures based on  $H\alpha$  line widths and either

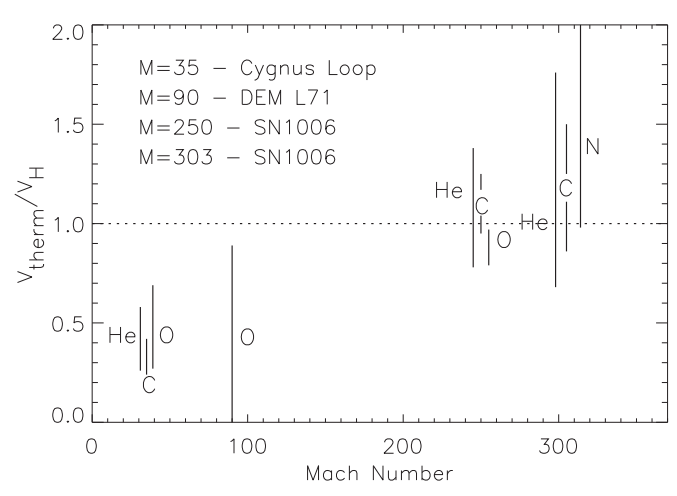


**Figure 10.** Line widths relative to hydrogen from various SNR observations, as indicated by the legend. The Mach numbers range from 35 for the Cygnus Loop to 303 for the SN 1006 bow shock studied in this paper. Each of the four observations has a single Mach number, but the elements are offset for clarity. The vertical lines indicate the extent of the  $1\sigma$  uncertainties. For the two positions in SN 1006, the element labels are placed at the best-fit values. The uncertainties for the Cygnus Loop and DEM L71 contain significant adjustments for Coulomb collisions and for the bulk expansion speed, respectively, so the best fit is less well defined. The horizontal dotted line at 1.0 corresponds to mass-proportional temperatures.

broad-to-narrow intensity ratios  $(I_b/I_n)$  or electron temperatures from X-rays indicate  $T_e/T_p < 0.1$  in the nearby section of the SN 1006 H $\alpha$  filament (Ghavamian et al. 2002; Long et al. 2003).

According to Figure 16 of Morlino et al. (2012), a ratio  $I_b/I_n=0.49\pm0.08$  that we found for H $\alpha$  is consistent with  $T_e/T_p<0.05$  for a 3000 km s<sup>-1</sup> shock, and that is in keeping with other determinations of equilibration for fast shocks (Ghavamian et al. 2013). The Morlino figure assumes a preshock neutral fraction of 0.5, which gives strong heating in the shock precursor, while the neutral fraction in the NW filaments of SN 1006 is about 0.1 (Ghavamian et al. 2002). Therefore, the precursor due to counterstreaming neutrals will be weak, and the  $I_b/I_n$  predictions may be underestimates in this case.

On the other hand, the IFU observations of the NW filament by Nikolić et al. (2013) showed that the  $I_b/I_n$  ratio exceeds 1 at the innermost edge of the  $H\alpha$  emission, while it is smaller out ahead of the brightest part of the filament. The slower shock is expected to have a higher  $I_b/I_n$  ratio (Morlino et al. 2012), but it is also plausible that a precursor contributes narrow-component  $H\alpha$  to all but the trailing edge of the filament structure. Our procedure of subtracting sky background from the portion of the slit just beyond the bow shock should remove any contribution from an extended precursor, and the observed value of  $I_b/I_n$  should be directly comparable to model predictions.

Overall, the low value of  $I_b/I_n$  indicates  $T_e/T_p$  below about 0.1, so the shock speed should be no more than 5% larger than the 3060 km s<sup>-1</sup> inferred with the assumption of  $T_e/T_p = 0.05$ .

## 5.5. Comparison with Other SNR Shocks

Figure 10 compares the ion thermal velocities relative to hydrogen with results obtained for SNR shocks with different Mach numbers. The dotted line corresponds to mass-proportional temperatures. The slowest shock, a 350 km s<sup>-1</sup> shock in the Cygnus Loop, shows He, C, and O velocity widths

consistent with  $1/m_i^{1/2}$ , i.e., ion temperatures consistent with the proton temperature (Raymond et al. 2015a). The 900 km s<sup>-1</sup> shock in DEM L71 shows an oxygen temperature less than 0.8 times mass proportional (Ghavamian et al. 2007a). (The value for DEM L71 was also consistent with zero because of the uncertainty in the contribution of the bulk expansion velocity to the line width.) The 2500 km s<sup>-1</sup> shock in SN 1006 somewhat to the NW of the bow shock studied here shows temperatures consistent with mass proportional (Raymond et al. 1995; Korreck et al. 2004).

As shown in Table 3 and Figure 10, the best-fit ion temperatures at the SN 1006 bow shock are somewhat higher than the mass-proportional values, but they lie within the measurement uncertainties. The  $T_i/T_p$  ratios are consistent with the values for the lower Mach number shock in SN 1006, but clearly higher than those in the slower Cygnus Loop shock. This is perhaps analogous to the electron–ion equilibration situation, in that  $T_e/T_p$  is close to 1 in the Cygnus Loop shocks, but less than 0.1 in SN 1006. The dependence of  $T_e/T_i$  on Mach number is shown by Ghavamian et al. (2013).

#### 5.6. Particle Acceleration

Global estimates suggest that of order 10% of SNR shock kinetic energy is transferred to cosmic rays. The NW section of SN 1006 is faint in radio and shows no X-ray synchrotron emission apart from the patch of emission located about 30" ahead of the bow shock we are studying. We therefore think it unlikely that a substantial fraction of the shock energy goes into cosmic rays. Nikolić et al. (2013) invoked nonthermal protons as an explanation for the variation in  $I_b/I_n$  within the IFU field of view located NE of the bow shock discussed here, so some particle acceleration may occur and the shock speeds and distance estimates would correspondingly increase. An upper limit on the particle acceleration efficiency can be derived from an upper limit on the shock speed and a lower limit on the proton temperature from the H $\alpha$  profile. Burleigh et al. (2000) give an upper limit to the distance of the Schweizer-Middleditch star (which must be behind SN 1006 because it shows absorption lines from the ejecta) of 2.10 kpc, which combined with our proper-motion upper limit of 0."35 yr<sup>-1</sup> implies an upper limit to the shock speed of 3560 km s<sup>-1</sup>. The lower limit to the H $\alpha$ FWHM and the models of Morlino et al. (2013a) imply a lower limit to the effective shock speed of 2500 km s<sup>-1</sup>. The ratio is an upper limit to  $(1 + 8\epsilon/9)^{1/2}$ , so that  $\epsilon < 0.52$ . This limit is not surprising given the lack of synchrotron emission, but few such limits for SNR shocks are available.

Laming et al. (2014) discuss the instabilities in a magnetized cosmic-ray precursor that could lead to electron heating. A criterion for the excitation of lower hybrid waves in terms of ion and electron thermal speed,  $v_i$  and  $v_e$ , and cosmic-ray and ion densities,  $n_{CR}$  and  $n_i$ , is (their Equation (26))

$$\frac{0.78v_i}{c} < \frac{n_{CR}}{n_i \langle \gamma \rangle} < \frac{0.78v_e}{c},\tag{1}$$

which arises because the wavevector of maximum growth in the reactive instability depends on the cosmic-ray density, and this wavevector must fall in the range allowed for lower hybrid waves. When the average cosmic-ray Lorentz factor  $\langle \gamma \rangle$  is expressed in terms of its maximum value  $\gamma_{\rm max}$  and the ratio of the injection velocity for cosmic-ray acceleration  $v_{\rm inj}$  to the shock velocity  $v_s$ ,  $\langle \gamma \rangle \simeq (\ln \gamma_{\rm max} - 1)v_{\rm inj}/c + 1$ , and substituted into

the expression for  $\eta = P_{CR}/\rho v_s^2$  (Equation (A4) in Laming et al. 2014), we find

$$\eta = \frac{n_{CR}}{n_i} \frac{c^2}{v_s^2} \frac{\ln \gamma_{\text{max}} - 1}{3} = \frac{cv_{\text{inj}}}{v_s^2} \frac{(\ln \gamma_{\text{max}} - 1)^2}{3} \\
\times (2 \times 10^{-5} \to 10^{-3}),$$
(2)

which evaluates to  $(0.044 \rightarrow 2.2) \times v_{\rm inj}/v_s$ , where the range of values comes from the inequalities in Equation (1). The lower end of this range, combined with a minimum injection velocity  $v_{\rm inj} = 2v_s$ , gives  $\eta > 0.1$  at shocks with significant electron heating in a cosmic-ray precursor. Such heating would manifest itself as a departure from the  $1/v_s^2$  dependence uncovered by Ghavamian et al. (2007b) and very much seems to be absent at the NW filament of SN 1006, again suggesting a low cosmic-ray partial pressure (less than 10%) at this shock wave.

## 5.7. Comparison with Theoretical Predictions

Fuselier & Schmidt (1997) studied the relative heating of He<sup>2+</sup> and H<sup>+</sup> at Earth's bow shock, where typical Mach numbers are 2-6. They proposed a mechanism based on differential slowing of particles by the electric field in the shock. Some observational support for this level of selective heating comes from observations of low Alfvén Mach number shocks in the solar corona (Mancuso et al. 2002), but not for all events (Mancuso & Avetta 2008). For a perpendicular shock, which is believed to be appropriate for the NW filament, their Equation (6) implies  $T_i/T_p = 4.8$ , 2.45, 2.29, and 2.07 (or  $m_p T_i / m_i T_p = 1.2, 0.2, 0.16, \text{ and } 0.13)$  for He, C, N, and O, respectively, for a strong shock with a compression ratio of 4. The relatively low mass-to-charge ratio of singly ionized He leads to a high predicted  $T_{\rm He}$ , which agrees with the observations, but the C and N predictions are too low compared to the SN 1006 observations.

Zimbardo (2011) computed the preferential heating of heavy ions by shocks based on reflection from the shock and acceleration in the motional electric field,  $V \times B$ . He predicted  $T_i = 1.5m_i$  to  $2m_i$  for He and O ions in a perpendicular shock and that the temperatures would be strongly anisotropic, so that the observed temperature would depend on the angle between the line of sight and the magnetic field. The temperatures of He and N observed in SN 1006 are consistent with the preferential heating predicted by Zimbardo (2011) within large error bars, but the temperatures of C and O are not. However, the Mach number of the SN 1006 shock is far larger than the shocks that Zimbardo (2011) considered.

The measured temperatures show no indication of preferential heating of the heavier ions, but neither do they indicate any transfer of energy among different species leading toward equal ion temperatures. This is somewhat similar to the results for  $T_e/T_p$ , which show that very little of the proton kinetic energy is transferred to the electrons.

### 6. Summary

We have observed a 3000 km s<sup>-1</sup> shock in SN 1006 in the UV with COS and in the optical with IMACS on Magellan to study the ion-ion equilibration and the particle velocity distributions in a fast collisionless shock. Based on its location in the NW filament, the shock is probably quasi-perpendicular, and based on the lack of nonthermal X-ray or radio emission, it

probably does not accelerate particles efficiently. We find that the kinetic temperatures of He, C, and N are consistent with  $T_i = (m_i/m_p)T_p$ , as would occur if a fraction of the shock speed of each particle is thermalized when it passes through the shock and there is no sharing of energy among different particle species. That is very far from thermal equilibrium, in which all the temperatures are the same. Within the measurement uncertainties, the observations are compatible with transfer of up to 25% of the energy from heavier species to protons or some preferential heating of the heavier species. These mass-proportional temperatures are similar to the result for a 2500 km s<sup>-1</sup> shock in SN 1006, but very different from the temperatures close to thermal equilibrium seen in the 350 km s<sup>-1</sup> shock in the Cygnus Loop.

The question of electron heating in the shock is closely related to the ion-ion thermal equilibration, although different plasma waves would be responsible for transferring energy from ions to electrons than those that would transfer energy among ion species. The intensity ratio of the broad and narrow components of  $H\alpha$  is about 0.5, which is compatible with the models of Morlino et al. (2013a) for 3000 km s<sup>-1</sup> shocks, but those models assume a much higher neutral fraction than is appropriate for SN 1006. The predicted values of  $I_b/I_n$  for a 3000 km s<sup>-1</sup> shock of van Adelsberg et al. (2008), which did not include a precursor, are significantly higher than observed for both Case A and Case B. The small observed value of  $I_b/I_n$ is similar to what was seen in the NW part of SN 1006 in the region where a photoionization precursor may enhance the narrow component, but in our case that contribution should be removed as part of the background. The small  $I_b/I_n$  could result from precursor emission very close to the shock, analogous to that reported in Tycho (Lee et al. 2010) and the Cygnus Loop (Medina et al. 2014; Katsuda et al. 2016).

The  ${\rm H}\alpha$  broad component is poorly fit by a Gaussian, indicating a non-Maxwellian velocity distribution of broad-component H atoms. This may result from the velocity dependence of the charge transfer cross section, from a non-Maxwellian proton distribution such as a  $\kappa$ -distribution, or from a strong precursor contribution. Given the probable low acceleration efficiency of the shocks in the NW filament of SN 1006, the latter two explanations seem less likely.

Our measured proper motion and the shock speed given by the broad component width and the models of Morlino et al. (2013a) yield a distance of 1.85  $\pm$  0.25 kpc if little energy goes into cosmic rays. The H $\alpha$  intensity is compatible with the pre-shock density range 0.15–0.3 cm<sup>-3</sup> of Heng et al. (2007) and the pre-shock neutral fraction of 0.1 of Ghavamian et al. (2002).

We thank Paule Sonnentrucker and the STScI staff for making last-minute pointing adjustments for the *HST* COS observations, and the Magellan Observatory staff for their excellent support during our run there. We also thank Brian Williams of STScI for the code we used to measure the optical proper motions. This work was supported by Guest Investigator grant *HST*-GO-13435.001 from the Space Telescope Science Institute and by Basic Research funds of the CNR (J.M.L.). P.F.W. acknowledges additional support from the NSF through grant No. AST-1714281.

Facilities: HST(COS), Magellan:Baade (IMACS), Gemini:

*Software:* IRAF (Tody 1986, 1993), COSMOS (http://code.obs.carnegiescience.edu/cosmos).

# Appendix A Non-Gaussian $H\alpha$ Profile

It is likely that the departure of the  $H\alpha$  profile results from the velocity dependence of the charge transfer cross section (Heng & McCray 2007; Morlino et al. 2013a), but here we discuss several other possibilities presented by Raymond et al. (2010).

Range of shock speeds: The effective shock speeds and bulk velocities due to the bow shock geometry were discussed above. For a shock propagating through a clumpy medium, a large range of shock speeds, and hence pre-shock densities if the ram pressure is constant, would be required to match both the full extent of the  $H\alpha$  broad component and the extra emission near the core. A fit with a narrow component and two broad-component Gaussians gives  $\chi^2=3.8$  and a good visual match to the profile with line widths of 1300 and 3200 km s<sup>-1</sup> for the intermediate and broad components. In this case, the dense clumps would have to be so small that they would not disturb the smooth, sharp morphology of the  $H\alpha$  filament. Clumps with a factor of 6 density contrast and scales of  $10^{16}$  cm or less could produce the emission near the line core. Overall, this seems to be a very unlikely explanation.

Pickup ions: Raymond et al. (2008) discussed the observable effects of pickup ion behavior in Balmer line filaments. Neutrals that pass through the shock become ionized in the downstream gas, and they behave like the pickup ions observed in the solar wind (Williams & Zank 1994; Isenberg 1995). The velocity component parallel to the magnetic field is conserved, while the perpendicular component becomes first a ring beam in velocity space and then a hollow shell. If those ions experience charge transfer with other neutrals, they produce a population of neutrals with the pickup ion velocity distribution. Because the neutral fraction in the NW filaments of SN 1006 is small (Ghavamian et al. 2002), the number of pickup ions is small and the probability of a second charge transfer event is small, so the H $\alpha$  produced in this way will be very weak, unlike in Tycho's SNR. Moreover, the perpendicular shocks in the NW filament will produce pickup ions with nearly the same velocity width as the ordinary thermal particles, and they cannot account for the intermediate velocity component that would be needed to explain the extra emission near line center.

We note that pickup ions could also affect the He II line profile, because some of the helium may be neutral when it encounters the shock. Unlike in the case of hydrogen, the line we observe can be produced by the pickup ions themselves, rather than requiring a second charge transfer event. On the other hand, very little carbon is neutral when it reaches the shock. Carbon in grains is gradually sputtered away in the post-shock gas, and betatron acceleration of the grains (Spitzer 1976) would imply a broad line, but the sputtering occurs over a broad region behind the shock (Raymond et al. 2013; Winkler et al. 2013), and the contribution to the line profile within the COS aperture is therefore modest.

*Power-law tail:* Raymond et al. (2010) were able to fit the  $H\alpha$  profile of a shock in Tycho's SNR with a  $\kappa$  distribution, which is basically a Maxwellian core with a power-law tail. A small value of  $\kappa$ , meaning a very strong tail, was required. A  $\kappa$  distribution might match the extra emission at highly redshifted

velocities, but it would not match the red-blue asymmetry observed in SN 1006, and it would not produce the extra emission near line center unless the temperature of the  $\kappa$ distribution were very low. The best fit of a narrow component plus a  $\kappa$  distribution to the H $\alpha$  profile gives  $\chi^2 = 4.3$ , considerably better than the value of 9.2 for the assumption of a single Gaussian broad component. Visually, the  $\kappa$ distribution fit greatly reduces the residuals near the center of the broad component and in the far wings. The best-fit  $\kappa$  is 2.1, but the values of  $\kappa$  and  $\theta$ , which is the square of the characteristic speed, trade off against each other in such a way that neither is constrained well. The small best-fit value of  $\kappa$ would indicate that a large fraction of the energy is contained in the power-law tail. That is hard to reconcile with weakness of synchrotron emission in the NW filament, but it is possible that only ions, and not electrons, are accelerated.

Precursor emission: Nonradiative shocks have photoionization precursors that can heat the upstream gas and might account for the 20 km s<sup>-1</sup> width of the narrow component observed in SN 1006 (Sollerman et al. 2003). Shocks can also have cosmic-ray precursors, which are required in the diffusive shock acceleration model, and they can have precursors owing to broad-component neutrals that overtake the shock and deposit their energy upstream (Hester et al. 1994; Smith et al. 1994). Gas in the precursor is compressed, accelerated, and heated, and the cosmic-ray precursor contains strong plasma turbulence. Charge transfer between protons and neutrals in the precursor heats the neutrals, so that narrow component line widths of 30–40 km s<sup>-1</sup> are observed (Medina et al. 2014; Knežević et al. 2017). If the heating by backstreaming neutrals is strong, an intermediate component can be formed close to the shock, and a line width as high as  $300 \text{ km s}^{-1}$  is predicted (Morlino et al. 2012). This intermediate component has been detected in a somewhat slower shock in Tycho's SNR with a width of about 190 km s<sup>-1</sup> (Knežević et al. 2017).

However, the pre-shock neutral fraction in the NW filaments of SN 1006 is only 10% (Ghavamian et al. 2002), which means that there are few broad component neutrals to flow upstream through the shock and correspondingly less heating in the precursor. Strong heating might occur in a cosmic-ray precursor, and we note that the hard X-ray emission seen in the bottom right panel of Figure 1 could suggest some particle acceleration in this region. The heating in the cosmic-ray precursor might be relatively strong owing to the pickup ion behavior of the incoming neutrals (Ohira & Takahara 2010; Raymond et al. 2011) or secondary shocks (Drury & Falle 1986).

The three-Gaussian fits gave FWHM around 1300 km s<sup>-1</sup> for the intermediate component and 3200 km s<sup>-1</sup> for the broad component. That would correspond to a shock speed of 4200 km s<sup>-1</sup> according to the models of Morlino et al. (2013a) and a precursor effective temperature (proton temperature plus turbulent speed added in quadrature) above  $3 \times 10^7$  K. The total intensity of the intermediate component is close to 40% that of the broad component, suggesting significant electron heating in the precursor if that is the correct picture. It should be borne in mind, however, that both the line widths and relative intensities are poorly constrained because of the strong correlations among the parameters in the three-Gaussian fits.

Overall, there is no obvious interpretation for the apparently non-Gaussian shape of the broad component of  $H\alpha$ . On the other hand, there is no reason to expect a Maxwellian velocity

distribution in a collisionless shock in the first place. Correlation among the parameters of these more complex fits results in elongated contours in the  $\chi^2$  plots such that the parameters are poorly constrained. Therefore, we use the single-Gaussian fit to determine the FWHM for use with the line widths predicted by Morlino et al. (2013a) to measure the shock speed and the implied thermal velocity for comparison with the widths of the UV lines.

# Appendix B Shocked Ion Distributions: Microphysics

Up to now we have discussed shocked ion properties purely in terms of the Rankine–Hugoniot jump conditions for thermodynamic variables like temperature and density. We have fitted spectra assuming Gaussian line profiles, but Table 3 and Figure 5 indicate that this is perhaps not justified. Here we sketch out how the shocked ion distribution function may be related to properties of the post-shock turbulence, and we indicate how Maxwellian or other particle distribution functions might result. We start from the Fokker–Planck equation in spherical coordinates for the particle distribution function f (e.g., Melrose 1986),

$$\frac{df}{dt} = \frac{1}{p^2} \frac{\partial}{\partial p} \left[ p^2 \left\{ A_p f + D_{pp} \frac{\partial f}{\partial p} + D_{p\alpha} \frac{\partial f}{\partial \alpha} \right\} \right] 
+ \frac{1}{\sin \alpha} \frac{\partial}{\partial \alpha} \left[ \sin \alpha \left\{ A_{\alpha} f + D_{\alpha p} \frac{\partial f}{\partial p} + D_{\alpha \alpha} \frac{\partial f}{\partial \alpha} \right\} \right], \quad (3)$$

where p and  $\alpha$  are particle momentum and pitch angle, respectively,  $-A_p$  and  $-A_\alpha$  are coefficients of dynamical friction, and  $D_{pp}$ ,  $D_{p\alpha}$ , and  $D_{\alpha\alpha}$  are diffusion coefficients in momentum space. Then integrating over pitch angles and in steady-state conditions,

$$\int_{0}^{\pi} \frac{df}{dt} \sin \alpha d\alpha = \frac{1}{p^{2}} \frac{\partial}{\partial p} \left[ p^{2} \left\{ \int_{0}^{\pi} A_{p} f \sin \alpha d\alpha + \int_{0}^{\pi} D_{pp} \frac{\partial f}{\partial p} \sin \alpha d\alpha \right\} \right] = 0$$
 (4)

if f is isotropic. The diffusion coefficient in the presence of transit time damping is

$$D_{pp} = \int \frac{8\pi^2 q^2}{\hbar \omega} \frac{V_A^2}{2c^2} \frac{v^2 \sin^2 \alpha}{4} \delta(\omega - k_{\parallel} v_{\parallel}) \times \left( \hbar k_{\parallel} \frac{\partial p}{\partial p_{\parallel}} \right)^2 \frac{U(\mathbf{k})}{\hbar \omega} \frac{d^3 \mathbf{k}}{(2\pi)^3}, \tag{5}$$

where  $\omega$  and  $k_{\parallel}$  are the wave frequency and parallel (i.e., along the ambient magnetic field, B) wavevector, respectively.  $U(\mathbf{k})$  is the wave energy density per unit volume in k-space, so that the total wave energy density in terms of the perturbed magnetic field  $\delta B^2/8\pi = \int U(\mathbf{k})d^3\mathbf{k}/(2\pi)^3$ . The particle speed is v, its parallel component is  $v_{\parallel}$  (similarly for momentum),  $V_A$  is the Alfvén speed, q is the particle charge, and c is the speed of light. This evaluates to

$$D_{pp} = \frac{\pi q^2 V_A^2 \sin^2 \alpha}{8v_{\parallel} c^2} \frac{\partial \delta B^2(k_{\parallel} = \omega/v_{\parallel})}{\partial k_{\parallel}}.$$
 (6)

We write  $\partial \delta B^2(k_{\parallel}=\omega/v_{\parallel})/\partial k_{\parallel}$  to represent the wave energy density at  $k_{\parallel}=\omega/v_{\parallel}$ , and this is always positive. Taking  $A_p=p\Omega$ , and adding a thermal diffusion coefficient  $p_t^2\Omega$  to the expression above, where the cyclotron frequency  $\Omega=qB/mc$ , the steady-state Fokker–Planck equation integrated over  $\alpha$  becomes

$$pf + \left\{ p_t^2 + \frac{\pi q^2 V_A^2}{3\nu_{\parallel} c^2 \Omega} \frac{\partial \delta B^2 (k_{\parallel} = \omega / \nu_{\parallel})}{\partial k_{\parallel}} \right\} \frac{\partial f}{\partial p} = 0.$$
 (7)

With  $\partial \delta B^2(k_{\parallel}=\omega/v_{\parallel})/\partial k_{\parallel}v_{\parallel}\sim\delta B^2/\omega$  and independent of v, this integrates to a Maxwellian,  $\exp{(-v^2/2v_t^2)}$  with  $v_t^2=p_t^2/m^2+(\pi V_A^2\Omega/3\omega)(\delta B^2/B^2)$ . The last term matches with the Rankine–Hugoniot relation if  $(\Omega/\omega)(\delta B^2/B^2)=9v_s^2/16\pi V_A^2$  and gives the same  $v_t$  for different ions if  $\Omega\partial\delta B^2(k_{\parallel}=\omega/v_{\parallel})/\partial k_{\parallel}$  is constant. In converting their motion toward the shock into the shocked distribution functions, ions of a given  $\Omega$  clearly share energy among themselves, but apparently not with ions of a different  $\Omega$ , since observations show all species having the same post-shock thermal velocity. This reinforces the idea that ions of a particular species all interact with the same set of waves, which are distinct from the sets of waves interacting with ions of different species.

If  $\delta B^2(\bar{k}_{\parallel} = \omega/\nu_{\parallel})$  depends on  $\nu$ , then other functional forms for f are possible. In particular, if  $\delta B^2(k_{\parallel} = \omega/\nu_{\parallel}) \propto k^{-2} \propto \nu^2$ , then a so-called kappa-distribution results,

$$f \propto \left[ p_t^2 + \frac{p^2}{2\kappa} \right]^{-\kappa},\tag{8}$$

with in this case

$$\kappa = \frac{3}{2\pi} \frac{\omega}{\Omega} \frac{v^2}{V_A^2} \frac{B^2}{\delta B^2},\tag{9}$$

which evaluates to a number of order 1–10, depending on assumptions made. Here  $p_t$  represents the thermal part of the distribution, not specified by this argument, and the turbulence gives rise to the nonthermal part. Post-shock turbulence initially with  $\delta B^2(k_{\parallel}=\omega/v_{\parallel})$  independent of v and then evolving to  $\propto v^2$  could establish an initial shocked ion distribution as a Maxwellian and then excite the nonthermal tail.

## ORCID iDs

J. C. Raymond https://orcid.org/0000-0002-7868-1622
 W. P. Blair https://orcid.org/0000-0003-2379-6518
 J. M. Laming https://orcid.org/0000-0002-3362-7040

#### References

Bamba, A., Yamazaki, R., Ueno, M., & Koyama, K. 2003, ApJ, 589, 827
Berdichevsky, D., Geiss, J., Gloeckler, G., & Mall, U. 1997, JGR, 102, 2623
Broersen, S., Vink, J., Miceli, M., et al. 2013, A&A, 552, 9
Burleigh, M. R., Heber, U., O'Donaghue, D., & Barstow, M. 2000, MNRAS, 356, 585
Cargill, P. J., & Papadopoulos, K. 1988, ApJL, 329, 29
Chevalier, R. A., Kirshner, R. P., & Raymond, J. C. 1980, ApJ, 235, 186

Chevalier, R. A., & Raymond, J. C. 1978, ApJL, 225, L27
Del Zanna, G., Dere, K. P., Young, P. R., Landi, E., & Mason, H. E. 2015,

Drury, L. O'C, & Falle, S. A. E. G. 1986, MNRAS, 223, 353

```
Fuselier, S. A., & Schmidt, W. K. H. 1997, JGRA, 102, 11273
Gaia Collaboration, Prusti, T., de Bruijne, J. H. J., et al. 2016, A&A, 595, A1
Ghavamian, P., Blair, W. P., Sankrit, R., Raymond, J. C., & Hughes, J. P.
   2007a, ApJ, 664, 304
Ghavamian, P., Laming, J. M., & Rakowski, C. E. 2007b, ApJL, 654, L69
Ghavamian, P., Raymond, J. C., Hartigan, P., & Balir, W. P. 2000, ApJ,
   535, 266
Ghavamian, P., Raymond, J. C., Smith, R. C., & Hartigan, P. 2001, ApJ,
   547, 995
Ghavamian, P., Schwartz, S. J., Mitchell, J., Masters, A., & Laming, J. M.
   2013, SSRV, 178, 633
Ghavamian, P., Winkler, P. F., Raymond, J. C., & Hartigan, P. 2002, ApJ,
   572, 888
Hamilton, A. J. S., Fesen, R. A., & Blair, W. P. 2007, MNRAS, 381, 771
Hamilton, A. J. S., Fesen, R. A., Wu, C.-C., Crenshaw, D. M., & Sarazin, C. L.
   1997, ApJ, 481, 838
Hamuy, M., Walker, A. R., Suntzeff, N. B., et al. 1992, PASP, 104, 533
Heng, K. 2010, PASA, 27, 23
Heng, K., & McCray, R. 2007, MNRAS, 654, 923
Heng, K., van Adelsberg, M., McCray, R., & Raymond, J. C. 2007, ApJ,
   668, 275
Hester, J. J., Raymond, J. C., & Blair, W. P. 1994, ApJ, 420, 721
Isenberg, P. A. 1995, RvGeo, 3, 623
Katsuda, S., Long, K. S., Petre, R., et al. 2013, ApJ, 763, 85
Katsuda, S., Maeda, K., Ohira, Y., et al. 2016, ApJL, 819, 32
Knežević, S., Läsker, R., van de Ven, G., et al. 2017, ApJ, 846, 167
Kohl, J. L. 1997, SoPh, 175, 613
Korreck, K. E., Raymond, J. C., Zurbuchen, T. H., & Ghavamian, P. 2004,
   ApJ, 615, 280
Korreck, K. E., Zurbuchen, T. H., Lepri, S. T., & Raines, J. M. 2007, ApJ,
  659, 773
Koyama, A., Petre, R., Gotthelf, E. V., et al. 1995, Natur, 378, 255
Laming, J. M., Hwang, U., Ghavamian, P., & Rakowski, C. 2014, ApJ, 790, 11
Laming, J. M., Raymond, J. C., McLaughlin, B. M., & Blair, W. P. 1996, ApJ,
  472, 267
Lee, J.-J., Raymond, J. C., Park, S., et al. 2010, ApJL, 715, L146
Long, K. S., Reynolds, S. P., Raymond, J. C., et al. 2003, ApJ, 586, 1662
Mancuso, S., & Avetta, D. 2008, A&A, 677, 683
Mancuso, S., Raymond, J. C., Kohl, J., et al. 2002, A&A, 383, 267
Medina, A., Raymond, J. C., Edgar, R. E., et al. 2014, ApJ, 791, 30
Meier, R. 1991, SSRV, 58, 1
Melrose, D. B. 1986, Instabilities in Space and Laboratory Plasmas
   (Cambridge: Cambridge Univ. Press)
Morlino, G., Bandiera, R., Blasi, P., & Amato, E. 2012, ApJ, 760, 137
Morlino, G., Blasi, P., Bandiera, R., & Amato, E. 2013a, A&A, 558, 25
Morlino, G., Blasi, P., Bandiera, R., Amato, E., & Caprioli, D. 2013b, A&A,
   557, 142
Nikolić, S., van de Ven, G., Heng, K., et al. 2013, Sci, 340, 45
```

```
Raymond, J. C. 1991, PASP, 103, 781
Raymond, J. C., Blair, W. P., & Long, K. S. 1995, ApJL, 454, L31
Raymond, J. C., Edgar, R. J., Ghavamian, P., & Blair, W. P. 2015a, ApJ,
  805, 152
Raymond, J. C., Edgar, R. J., Ghavamian, P., & Blair, W. P. 2015b, ApJ,
  814, 165
Raymond, J. C., Ghavamian, P., Williams, B. J., et al. 2013, ApJ, 778, 161
Raymond, J. C., Isenberg, P. A., & Laming, J. M. 2008, ApJ, 682, 408
Raymond, J. C., Korreck, K. E., Sedlacek, Q. C., et al. 2007, ApJ, 659, 1257
Raymond, J. C., Thompson, B. J., St. Cyr, O. C., et al. 2000, GRL, 27,
  1439
Raymond, J. C., Vink, J., Helder, E. A., & de Laat, A. 2011, ApJL, 731, L14
Raymond, J. C., Winkler, P. F., Blair, W. P., Lee, J.-J., & Park, S. 2010, ApJ,
Rothenflug, R., Ballet, J., Dubner, G., et al. 2004, A&A, 425, 121
Schneiter, E. M., Velázquez, P. F., Reynoso, E. M., Esquivel, A., &
  De Colle, F. 2017, MNRAS, 449, 88
Schwartz, S. J., Thomsen, M. F., Bame, S. J., & Stansberry, J. 1988, JGR, 93,
   12923
Schweizer, F., & Middleditch, J. 1980, ApJ, 241, 1039
Shimoda, J., Inoue, T., Ohira, Y., et al. 2015, ApJ, 803, 98
Shimoda, J., Ohira, Y., Yamazaki, R., Lmaing, J. M., & Katsuda, S. 2017,
  preprint
Smith, R. C., Kirshner, R. P., Blair, W. P., & Winkler, P. F. 1991, ApJ,
  375, 652
Smith, R. C., Raymond, J. C., & Laming, J. M. 1994, ApJ, 420, 286
Sollerman, J., Ghavamian, P., Lundqvist, P., & Smith, R. C. 2003, A&A,
Spitzer, L. 1976, ComAp, 6, 177
Tanimori, T., Hayami, Y., Kamei, S., et al. 1998, ApJL, 497, L25
Tody, D. 1986, Proc.
                       IE, 627, 733
Tody, D. 1993, in ASP Conf. 52, Astronomical Data Analysis Software and
   Systems II, ed. R. J. Hannisch, R. J. V. Brissenden, & J. Barnes (San
  Francisco, CA: ASP), 173
Tracy, P. J., Kasper, J. C., Raines, J. M., et al. 2016, PRL, 116, 255101
van Adelsberg, M., Heng, K., McCray, R., & Raymond, J. C. 2008, ApJ,
  689, 1089
Velázquez, P. F., Schneiter, E. M., Reynoso, E. M., et al. 2017, MNRAS,
  466, 4851
Vink, J., Laming, J. M., Gu, M. F., Rasmussen, A., & Kaastra, J. S. 2003,
   ApJL, 587, 31
Williams, L. L., & Zank, G. P. 1994, JGR, 99, 19229
Winkler, P. F., Gupta, R., & Long, K. S. 2003, ApJ, 585, 324
Winkler, P. F., Williams, B. J., Blair, W. P., et al. 2013, ApJ, 764, 156
Winkler, P. F., Williams, B. J., Reynolds, S. P., et al. 2014, ApJ, 781, 65
Wu, C.-C., Leventhal, M., Sarazin, C. L., & Gull, T. R. 1983, ApJL, 269, 5
Zimbardo, G. 2011, P&SS, 59, 468
```

Ohira, Y., & Takahara, F. 2010, ApJL, 721, L43